Jets, Coronal "Puffs," and a Slow Coronal Mass Ejection Caused by an Opposite-polarity Region within an Active Region Footpoint

Alzate, N.; Morgan, H.

Published in:
Astrophysical Journal

DOI:
10.3847/0004-637X/823/2/129

Publication date:
2016

Citation for published version (APA):
Alzate, N., & Morgan, H. (2016). Jets, Coronal "Puffs," and a Slow Coronal Mass Ejection Caused by an Opposite-polarity Region within an Active Region Footpoint. *Astrophysical Journal*, *823*(2), 1-11. [129]. https://doi.org/10.3847/0004-637X/823/2/129

The Astrophysical Journal, 823:129 (11pp), 2016 June 1 doi:10.3847/0004-637X/823/2/129

JETS, CORONAL "PUFFS," AND A SLOW CORONAL MASS EJECTION CAUSED BY AN OPPOSITE-POLARITY REGION WITHIN AN ACTIVE REGION FOOTPOINT

N. Alzate and H. Morgan
Institute of Mathematics, Physics and Computer Science, Prifysgol Aberystwyth, Ceredigion, Cymru SY23 3BZ, UK; naa19@aber.ac.uk
Received 2015 December 24; accepted 2016 April 2; published 2016 May 31

ABSTRACT

During a period of three days beginning 2013 January 17, twelve recurrent reconnection events occur within a small region of opposing flux embedded within one footpoint of an active region, accompanied by flares and jets observed in EUV and fast and faint structureless "puffs" observed by coronagraphs. During the same period a slow structured CME gradually erupts, with one end anchored close to, or within, the jetting region. Four of the jet events occur in pairs—a narrow, primary jet followed within a few tens of minutes by a wider, more massive, jet. All the jets are slow, with an apparent speed of $\sim$100 km s^{-1}. The speed of the wide puffs in the coronagraph data is $\sim$300 km s^{-1}, and the timing of their appearance rules out a direct association with the EUV jetting material. The jet material propagates along large-scale closed-field loops and does not escape to the extended corona. The rapid reconfiguration of the closed loops following reconnection causes an outwardly propagating disturbance, or wave front, which manifests as puffs in coronagraph data. Furthermore, the newly expanded closed flux tube forms a pressure imbalance, which can result in a secondary jet. The reconnection events, through recurrent field reconfiguration, also leads to the gradual eruption of the structured flux tube appearing as the slow CME. Faint propagating coronal disturbances resulting from flares/jets may be common, but are usually obscured by associated ejections. Occasionally, the associated material ejections are absent, and coronal puffs may be clearly observed.

Key words: Sun: activity – Sun: corona – Sun: coronal mass ejections (CMEs) – Sun: flares

Supporting material: animations

1. INTRODUCTION

Studies linking jets to coronal phenomena are rare compared to the large number of observational and model studies of jets. Jets have a huge variation of observational characteristics and can arise from many different regions at the Sun. Common to all jets is their broad definition as rapid eruptions of material that are guided radially through the corona along flux tubes rooted in the photosphere (e.g., Moore et al. 2010), driven by reconnection between regions of opposite magnetic polarity (e.g., Shimojo et al. 2007). The association of jets with magnetic reconnection is well-established by models (e.g., Forbes & Priest 1985) and observations (e.g., Pariat et al. 2009). The trigger for reconnection is often a small region of emerging photospheric flux within an oppositely directed pre-existing field. For example, an important early MagnetoHydroDynamic (MHD) simulation of emerging flux by Forbes & Priest (1985) showed the formation of a region of closed loops and a current sheet, and the production of fast flows (i.e., jets) as the reconnection rate increased. More recent, advanced MHD simulations confirm the same basic mechanism for jet formation (e.g., Yokoyama & Shibata 1996; Moreno-Insertis & Galsgaard 2013).

Beyond these broad common characteristics, jets possess a plethora of different observational characteristics (size, density, bulk velocity, temperature, magnetic field strength). They are observed in many different wavelength regimes, and can occur in polar regions, coronal holes, and active regions (ARs). Coronal jets include X-ray jets, Extreme Ultra-violet (EUV) jets, Hα surges, EUV macrospicules, and Hα macrospicules (e.g., Shen et al. 2012; Priest 2014). The first extensive studies of jets were enabled by the X-ray observations of Yokhoh (e.g., Shibata et al. 1992). More recently, studies have been carried out using space- and ground-based observations including *TRACE*, *Hinode* and *STEREO* (e.g., Alexander & Fletcher 1999; Culhane et al. 2007; Patsourakos et al. 2008). Soft X-ray observations by *Yohkoh* revealed jets with temperatures of 3–8 MK, densities of (0.7–4) $\times$ 10^9 cm^{-3}, and velocities of 180–350 km s^{-1}. Reported jet bulk speeds range from tens to a thousand km s^{-1}. Similarly, the sizes of jets vary from tens to several hundred Mm. The temperature of the ejected plasma is $\sim$4 MK for X-ray jets, $\sim$1 MK for EUV jets and EUV macrospicules, and $\sim$100,000 K for Hα surges and Hα macrospicules (Moore et al. 2010). Efforts to classify the different characteristics of jets were made by Moore et al. (2010) (standard and blowout jets) and Nisticò et al. (2009) (Eiffel-tower, λ, and micro-CME jets).

There are several observational studies of recurring jets originating from the same emerging flux region near, or within, ARs (Chifor et al. 2008; Guo et al. 2013; Zhang & Ji 2014; Li et al. 2015). Most of these studies are recent since they are enabled by the regular, high-cadence observations of the Atmospheric Imaging Assembly (AIA, Lemen et al. 2012) aboard the *Solar Dynamic Observatory* (*SDO*). One example is the study carried out by Li et al. (2015) in which a series of recurring jets was observed in AR NOAA 11459 due to an emerging bipole, over a period of three hours in both EUV and soft X-rays, indicating material at different temperatures. Zhang & Ji (2014) describe in detail a series of three jets near AR NOAA 11259. Their observations show the jet material returning to the Sun with a near-parabolic trajectory.

Jets are manifested in observations of the extended corona by coronagraphs as narrow, fast, unstructured coronal mass ejections (CME). Vourlidas et al. (2013) identified a subset of smaller CMEs as "jet-CMEs." These are narrow CMEs of $\leqslant 40^\circ$ or less in width lacking a sharp front, detailed sub-

structure, or circular morphology. Coronagraph observations of jet CMEs were reported in the context of a polar coronal hole by Wang et al. (1998). Yu et al. (2014) tracked high-speed jet eruptions from the low corona into the inner heliosphere. They compared coronagraph images of jets with *Hinode* X-ray Telescope (XRT) observations and determined their speeds. Through analysis of the Solar Mass Ejection Imager (SMEI) data, the high-speed jets were tracked into the inner heliosphere from which mass and flow energies were determined. Their analysis of jetting material accelerated by the strong open magnetic fields adjacent to the jets was as previously suggested by Raouafi et al. (2008) and Tsuneta et al. (2008). Shen et al. (2012) describe a coronal blowout jet event which leads to the eruption of both jetting material (narrow ejection) and a filament or flux-rope (bubble-like) CME, both observed faintly in coronagraph images. They combine high-temporal and high-spatial-resolution observations at different wavelengths to reveal how external reconnection produces the jet-like CME and leads to the rising of a filament, while internal reconnection causes the bubble-like CME. Liu et al. (2015) present an analysis of a coronal jet and a CME observed through multiple wavelengths and at multiple observation points. These observations show that the CME is triggered by the jet, which later becomes the core of the CME.

This study describes observations of recurrent jetting activity from an AR, which leads to a sequence of propagating disturbances in the extended corona. Section 2 describes our observations of these events and the main set of instruments used in the study. Section 3 describes our data analysis in detail. Section 4 gives our best interpretation of the sequence of events and summarizes our conclusions.

2. OBSERVATIONS

Our study is based on the appearance of a series of rapid "puffs" and a cotemporaneous and cospatial slow eruption detected in white light coronagraph data over the course of 3 days just north of the west limb. EUV data show that the puffs are associated with a series of recurrent jets. This section describes these, and other, associated phenomena observed during the 3 day period in multiple instruments.

2.1. Slow and Impulsive Events

Over the course of ∼3 days starting on 2013 January 17, an interesting series of fast eruptions or puffs propagating in the northwest corona were observed by the Large Angle Spectrometric Coronagraph (LASCO, Brueckner et al. 1995) C2 instrument onboard the *Solar and Helispheric Observatory* (*SOHO*) satellite. Each of the fast eruptions (impulsive events) has been identified (Imp 1, Imp 2, etc.) and listed in Table 1. At the west limb during this period there is much activity, and selection of events is an important consideration. The 12 impulsive events are clearly identified in LASCO C2 over the three days. The first fast event occurs on 2013 January 17 starting at 03:09 UT. There is then a 23 hr respite before another fast event on 2013 January 18 02:18 UT. Following this event is a rapid series of fast or impulsive events occurring every two or three hours throughout 2013 January 18 until 20:11 UT. Another three events occur during the first half of 2013 January 19. Figure 1 shows LASCO C2 images of one of the impulsive events (IMP 6), labeled "F" in the images.

Table 1
Start Time of the Impulsive Events and Associated Phenomena for Several Instruments

Event	Date	LASCO	EUVI-A	AIA	SWAVES	*GOES*
1	17	03:09	02:35	02:51	02:54	03:00
2	18	02:18	01:45	01:42	-dg-	-ns-
3	18	05:06	04:45	04:45	04:45	04:42
4	18	07:30	07:00	06:42	07:00	-ns-
5	18	08:42	08:20	08:21	08:18	08:06
6	18	09:54	09:40	09:42	09:39	09:45
7	18	13:30	12:00	12:00	12:12	-ns-
8	18	15:42	-dg-	15:24	15:25	15:30:
9	18	20:11	20:00	20:00	20:00	-ns-
10	19	02:11	01:55	01:20	01:12	-ns-
11	19	06:23	-dg-	06:03	05:57	-ns-
12	19	10:46	10:25	10:51	10:27	-ns-

Note. Dates are for 2013 January. "-dg-" indicates a data gap while "-ns-" indicates no signature. Timings of flare brightenings are measured in EUV using the Extreme Ultra-violet Imagers (EUVI) of the Sun–Earth Connection Coronal and Heliospheric Investigation (SECCHI, Howard et al. 2002, 2008) on board *STEREO A* (Kaiser 2005) and by the Atmospheric Imaging Assembly (AIA; Lemen et al. 2012) on board the *Solar Dynamics Observatory* (*SDO*; Pesnell et al. 2012). Peaks in X-ray Intensity are measured by the *Geostationary Operational Environmental Satellite* (*GOES*) and type III radio bursts by *STEREO*/WAVES (SWAVES, Bougeret et al. 2008).

In the same region during the same period, a slow eruption gradually traveled through the LASCO C2 field of view (FOV). Figure 2 shows a time series of LASCO C2 observations over this period. The onset of the slow event is at 13:30:00 UT on the 18th and makes its way across the FOV in approximately 12–16 hr. At around 21:47:00 UT, a Figure 8-like structure is seen over the entire FOV in Figure 2(g). Figure 3 shows the slow event for LASCO C2 and in EUV data by the Sun Watcher using Active Pixel System Detector and Image Processing (SWAP) instrument aboard Projects for Onboard Autonomy (PROBA2, Halain et al. 2013; Seaton et al. 2013). The accompanying LASCO C2 movie (available in the electronic edition of the Astrophysical Journal), in particular, shows the very gradual initial eruption of this slow event. Its intermittent and gradual eruption seems to be linked to the series of fast eruptions. This structure is seen faintly in SWAP 171 Å observations at 13:29:06 UT on January 17th, more clearly viewed in the LASCO movie. In a movie generated using the 304 Å images, there is a shedding of material before the slow event that appears to fall back toward the Sun. This movie is also available in the electronic edition of the journal. This slow event is structured, and is likely a flux rope CME. Its formation and initial propagation is very gradual, and it is not associated with any clear filament eruption or any other low coronal signature of note. Although difficult to quantify, it appears as if the initial stages of the slow event's movement in the LASCO C2 data is dictated by the rapid series of puffs, that is, the propagation is intermittent, and the slow structure is "buffeted" by the passing of the fast events (see movie).

A height/time stack plot is shown in Figure 4 using slices of the DST-processed LASCO C2 data at the appropriate angular region of interest. The plot shows clearly the fast events (one is labeled "F") as bright streaks at an acute angle to the vertical (i.e., high speed), while the slow event (labeled "S") shows a very slow rise. Further study of the speed of the puffs will be made in a following section.

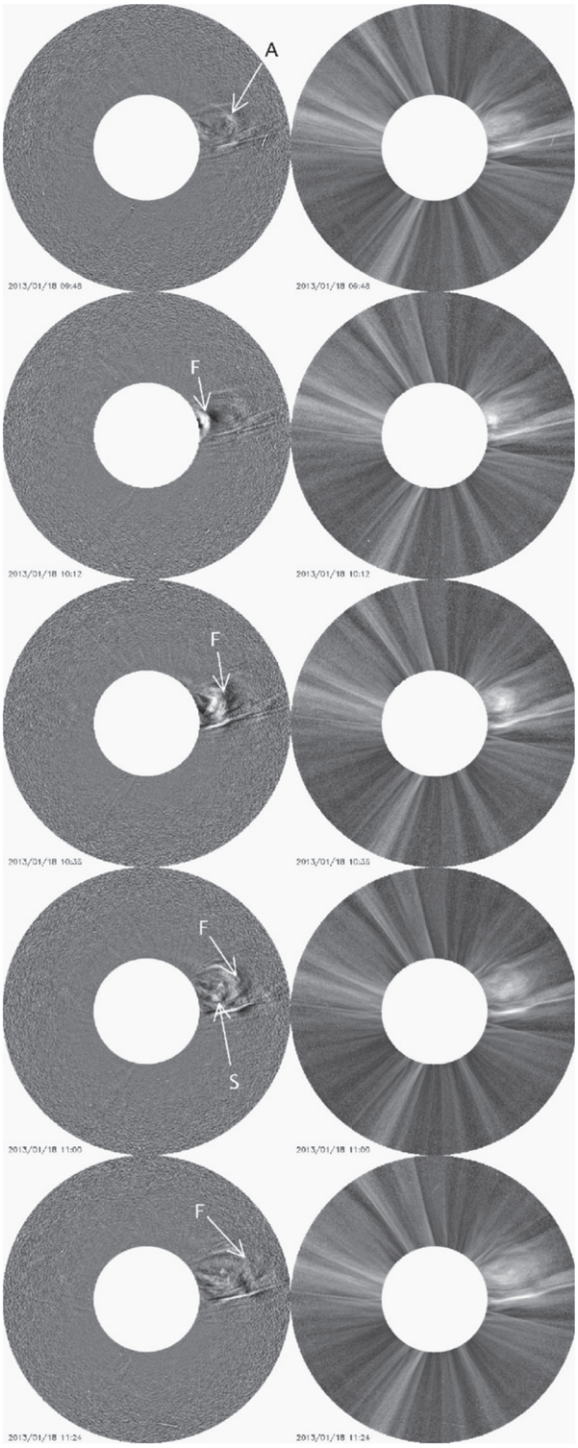

Figure 1. LASCO C2 dynamic (left column) and original (right column) time series images showing the course of propagation of one fast event on 2013 January 18 beginning at 09:45:00 UT. The fast event is labeled "F" and the slow event is labeled "S." Label "A" refers to the previous fast event that has yet to leave LASCO's FOV when the new event (F) enters. These observations have been processed with the Dynamic Separation Technique (DST; Morgan et al. 2012; Morgan 2015), which uses a spatial-temporal deconvolution method to separate the dynamic and quiescent components of the observation. The DST is used to better reveal the faint dynamic events, and gives superior results compared to simpler running- or base-difference methods. Unfortunately, the events are not clearly seen in the coronagraphs on board the *Solar Terrestrial Relations Observatory* (*STEREO*) Ahead (A) and Behind (B) spacecraft (Howard et al. 2008) nor in the LASCO C3 instrument.

Based on the LASCO C2 observations, there are several features of interest:

1. The fast events are faint and appear to have little structure except for a broad, faint front with an angular extent of $\sim 30^{\circ}$. They do not possess a classic 3-part eruption structure. As such, they can be described as puffs. Whether they are a propagating disturbance of pre-existing coronal material or an actual transport of new material is a difficult question which will be discussed.
2. During 2013 January 18, the rapid sequence of fast events means that the front of one fast eruption has not left the LASCO C2 FOV before another event enters the FOV. In Figure 1 the previous event is labeled "A."

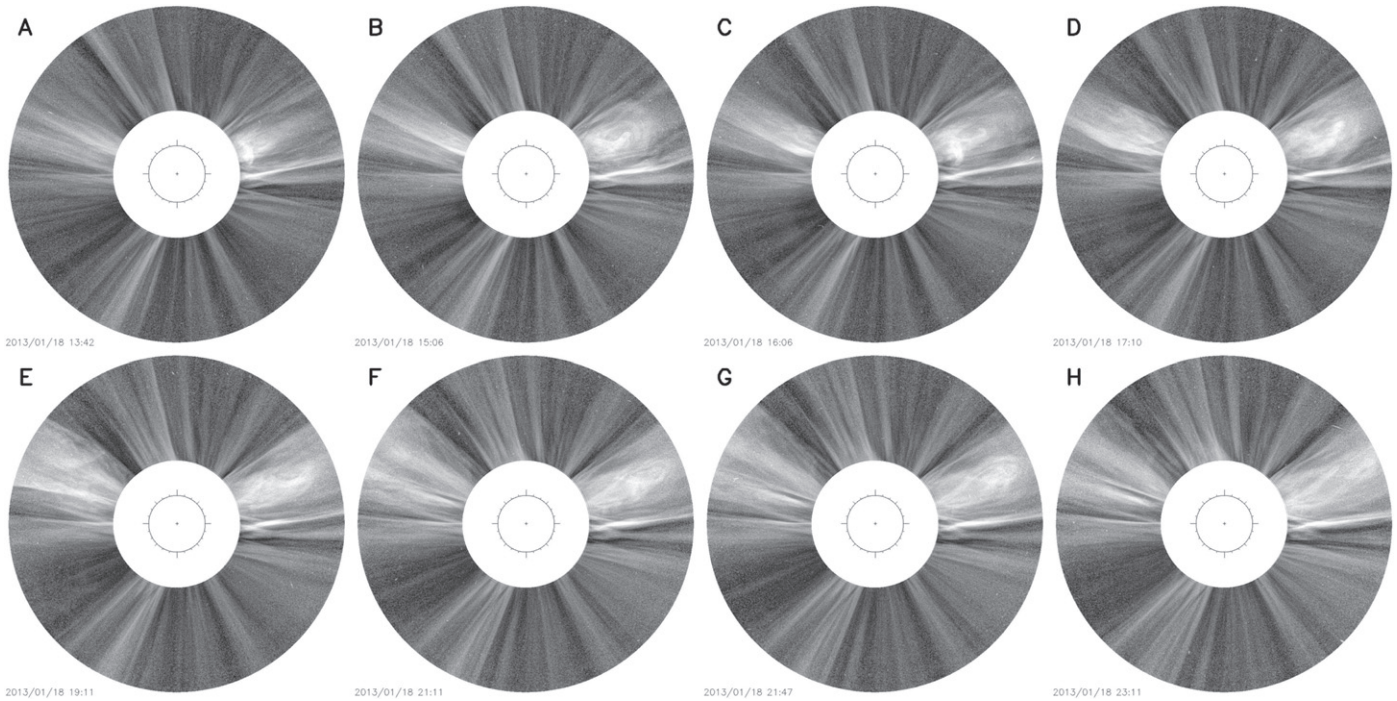

Figure 2. LASCO C2 images for a slow-event as it crosses the field of view on 2013 January 18 beginning at about 13:30:00 UT (A) until approximately 22:00:00 UT (H). LASCO C2 has a useful field of view (FOV) ranging from 2.2 to 6.0 $R_{\odot}$, and a spatial resolution of 11.4 arcsec pixel^{-1}. During the observational periods presented here, the cadence of LASCO C2 is ∼10 minutes in total brightness, using the most commonly used "orange" filter (broadband visible light) and clear polarizer channel. These images are processed using the Normalizing Radial Graded Filter (NRGF; Morgan et al. 2006) which removes the steep radial gradient of brightness in the images to better reveal structure, applied after appropriate removal of a long-term minimum background (Morgan 2015).

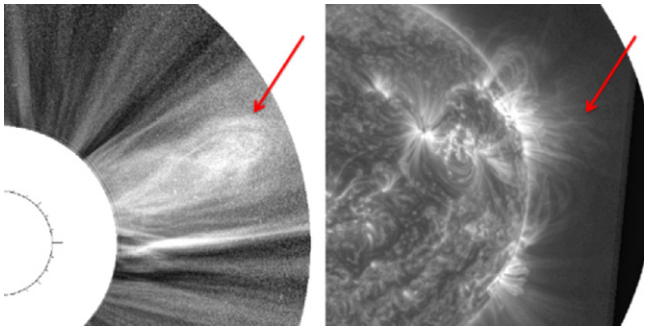

Figure 3. LASCO C2 image (left) showing the structure of the slow-event as it crosses the FOV at 21:47:00 UT on January 18. The image on the right (right) is from SWAP showing the same Figure-8-like structure. This image was taken at a wavelength of 171 Å on 2013 January 17 at 13:29:06 UT. SWAP provides images of the lower corona over a 54 arcmin FOV with 3.2 arcsec pixel^{-1} and a cadence of two minutes. It has a single 175 Å channel that provides observations of the solar corona approximately every 1–2 minutes. A movie showing the slow event as it makes its way across the LASCO C2 FOV is available in the electronic edition of the journal.

(An animation of this figure is available.)

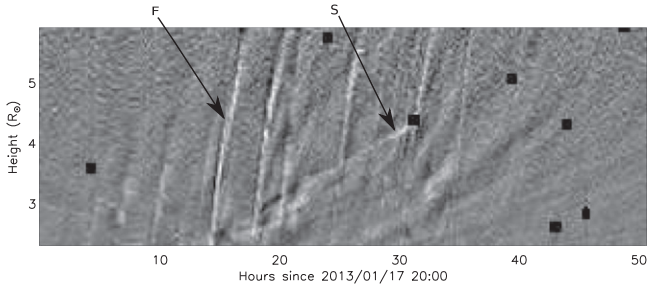

Figure 4. Height/time stack plot for the 50 hr interval (January 17–19) during which several fast events and one slow event took place. The slow event (labeled S) is shown as well as one of the fast events (labeled F).

3. The position of the slow eruption is labeled "S" in the figure. The fast event overtakes this slow eruption and seems to interact with it. In particular, as is most apparent from the movie, the slow eruption seems to be buffeted and encouraged to propagate outwards in intermittent steps by the fast eruptions. Whether this is a visual effect or a true interaction is discussed later.
4. The fast eruptions are fast and faint, and share their position in the images with the slow event and with the movement of more quiescent background coronal structures. This makes an estimate of their mass very difficult, although this is attempted later in this paper (see Table 2).

2.2. Flares and Jets from the Low Corona

This subsection presents observations by multiple instruments which show that the impulsive events are associated with a small region of opposing flux embedded within one footpoint of an AR which drives a series of flares (observed in radio, X-ray and EUV observations) and jets (observed in EUV).

The source of the fast events observed by LASCO C2 is a region of positive flux at the footpoint of a large AR. Figure 5(c) shows a Helioseismic Magnetic Imager (HMI, Scherrer et al. 2012) magnetogram of the AR. For a few days prior to the AR's passing of the limb, a small region of positive

Table 2
Kinematics and Masses for All Events

Event	EUVI Speed (km s^{-1})	Linear Speed (km s^{-1})	Acceleration (m s^{-2})	Mass (10^{11} kg)	F (10^{11} N)	F_g (10^{11} N)	$F - F_g$ (10^{11} N)
Slow	...	132 ± 41	−4	...	...	...	...
1	479	340 ± 6	−16	2.00	−31.6	−32.8	5.4
2	494	225 ± 105	−16	0.50	−7.9	−8.14	1.3
3	783	292 ± 40	−24	1.20	−28.2	−19.5	−6.0
4	544	197 ± 75	−4	0.80	−3.1	−13.0	11.7
5	747	296 ± 61	−5	2.90	−13.5	−47.2	40.1
6	1188	354 ± 45	−9	3.20	−27.8	−52.1	31.3
7	179	333 ± 51	−14	1.95	−26.4	−31.8	9.7
8	-dg-	468 ± 206	−34	2.00	−68.4	−32.6	−31.5
9	1530	443 ± 115	−32	3.00	−97.3	−48.9	−41.9
10	396	193 ± 131	−2	3.20	−7.7	−52.1	51.4
11	-dg-	448 ± 97	−21	0.40	−8.2	−6.52	−0.8
12	784	650 ± 35	−99	0.50	−49.5	−8.14	−40.3

Note. "Slow" denotes the slow event. EUVI speeds are calculated simply through the time difference between the appearance of a jet in the EUVI data and its subsequent first appearance in LASCO C2. Linear speed, acceleration, and mass are calculated from LASCO C2 data in the height range 2.2–6 $R_\odot$. "F" is the force calculated from the estimated mass and acceleration. "F_g" is the gravitational force for the given mass averaged over the C2 field of view. "$F - F_g$" gives a very approximate estimate of the net force acting outwards from the Sun as a mean over the LASCO C2 field of view.

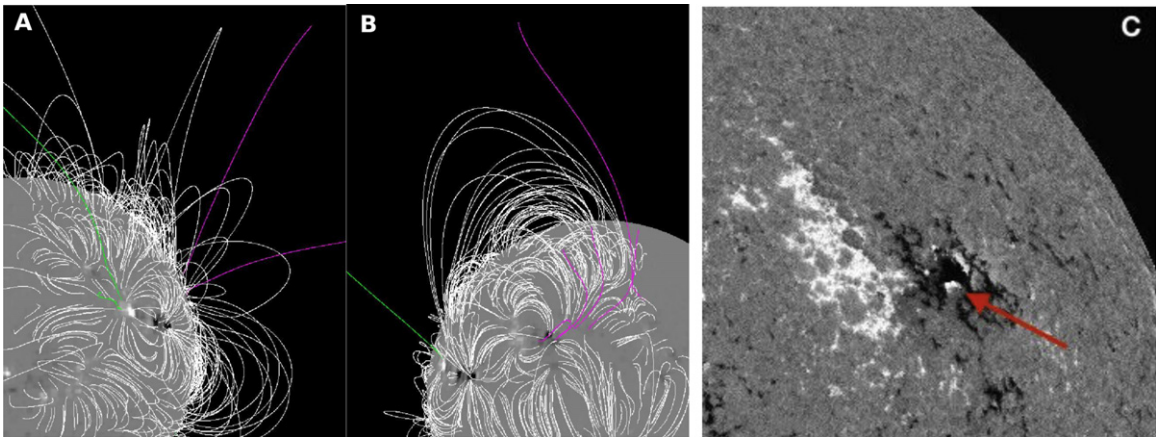

Figure 5. Magnetic field lines for the region of interest generated using a PFSS extrapolation for 2013 January 18 from (A) *SDO*'s and (B) EUVI A's perspective. (C) HMI/*SDO* magnetogram image of 2013 January 15, showing the active region of interest. The arrows point to embedded islands of positive flux in the active region's negative footpoint.

flux emerges within the western negative footpoint. This small yet persistent island of positive flux is driving considerable flaring and jetting activity. A potential field source surface (PFSS) extrapolation of the HMI synoptic observations (Schou et al. 2012) reveals that the westernmost negative footpoint of the AR is situated close to a small bundle of open field, as shown in Figures 5(a) and (b).

Figure 6 shows *GOES* and SWAVES data for the time of interest. Overplotted are the times of first appearance of the impulsive events observed by LASCO C2 (black dotted line), and associated jets by AIA (red dotted line) and EUVI-A (blue dotted line), corresponding to the timings listed in Table 1. Most of the events detected in EUV, and subsequently by LASCO C2, have an obvious correspondence to peaks in either or both *GOES* and SWAVES. This is confirmation that the embedded island of positive flux observed in the AR by HMI for several days prior to reaching the limb, is causing intermittent reconnection and a series of type III bursts. *GOES* observes X-ray brightenings for most events despite the base of the events being just behind the limb.

As listed in Table 1, each impulsive event is accompanied by a flare (as observed in EUV, and by SWAVES) and a coronal jet (as observed in EUV). One EUV sequence, as observed by AIA, is shown in Figure 7, for 2013 January 18 01:42. At this time, despite the very base of the region being just beyond the limb from AIA's perspective, the extreme brightening associated with the flare is clearly observed, as shown for several wavelength channels in Figures 7(a)–(c). The event is observed on the disk by EUVI-A, as shown in Figure 7(d). A running difference image (Figure 7(e)) shows streams of material jetting rapidly outwards along narrow paths from the small flaring region, as well as the brightening at the base of the region. Examples of several flares/jets as viewed by AIA and EUVI A are shown in Figure 8. Each event is similar, with a brief extreme brightening accompanied by eruption of material along a narrow path.

Four of the jet events show a two-stage jetting activity—a primary, narrow jet followed by a wider secondary jet which appears more like a "spray." Figure 9 shows details of impulsive event IMP 6 which is a clear example of this two-stage jetting activity seen in the AIA 304 Å channel. An initial

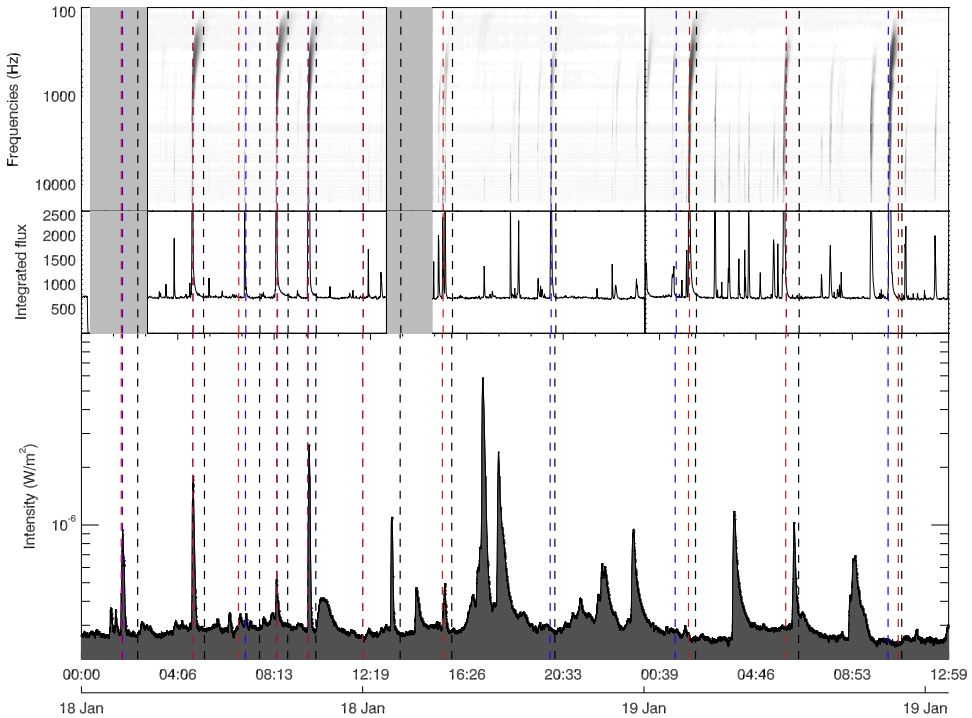

Figure 6. SWAVES (top) and *GOES* (bottom) data for 2013 January 18–19. Impulsive event times for LASCO (black), EUVI (blue), and AIA (red) are indicated by the dashed lines. SWAVES can detect coronal and interplanetary signatures of eruptions by measuring frequencies of 10 KHz to 50 MHz. *GOES* monitors solar X-ray intensity for the detection of flares.

very narrow jet (primary) raises rapidly from the flaring region. A few tens of minutes later, a broader spray-like jet (secondary) rises from the same region. This two-stage jetting activity is typical of Imp 2, 3, 6 and 10. The other Imp events do not show this two-stage process. Figure 10 shows time-differenced images from AIA 171 Å and EUVI 195 Å, showing the three primary phases of the Imp 2 jets. After the initial flare, a narrow jet is observed (top pair). A few minutes later, the time-differenced images (middle pair) show a broad depletion region (dark region), indicative of a loss of emission due to mass loss or absorption by dense material. From studying non-differenced images in the 304 Å and hotter channels, the latter explanation of absorption is most appropriate. Lastly, a broad jet is observed (lower pair).

The sequence of paired jet eruptions is similar to the EUV activity presented in a study of a simultaneously observed bubble and jet CME by Shen et al. (2012). Their detailed work presents a convincing interpretation for the formation of jet pairs in the lowest corona, with the initial reconnection forming the first narrow jet, which weakens the field overlying a small flux rope, which subsequently erupts as a small flux-rope CME. Certainly the cases of Imp 2, 3, 6 and 10 share similarities with the event of Shen et al. (2012), in that the jets occur in pairs, and that the initial jet is narrow and the secondary jet broader and denser. However, the association of the secondary jet with a bubble, or flux-rope, CME is not clear in the Imp events. In particular, the timing of the appearance of the puffs in the LASCO C2 FOV does not agree with the formation of a flux-rope CME during the secondary phase of the jet, as will be shown in Section 3.

3. DATA ANALYSIS

Using a manual point-and-click approach, height and time information is collected on all events in the AIA and LASCO C2 data. Figure 11 shows height–time profiles from AIA and LASCO C2 for four selected events (Imp 2, 3, 6 and 10). The red curves show the initial primary eruption of material, as tracked in AIA 304 Å channel images, immediately following the flare brightening. The blue curves show, for these four events, the associated, larger secondary eruption of material from the same region also tracked in AIA 304 Å channel. The black points track the puffs in the LASCO C2 images. There are several important points arising from these four events. While the brightening associated with the initial flare is obvious in all channels, only the 304 Å channel shows any obvious, easy-to-follow primary jets (red points) immediately following the flare. Time differencing is required to reveal the jets in the hotter channels—probably because they contain a lot of AR loops and other structure in the same region as the jets. The 304 Å channel is largely devoid of this structure, so the jets are more clearly observed. Comparison of images show that the timing of the appearance of the jets is similar in all channels. The secondary jets (blue points) occur a few minutes to a few tens of minutes after the primary jets. They are broader than the primary jets, appearing to spread more with height. The footpoint of the jets, as observed by EUVI A, is between 20° and 30° behind the limb. Assuming radial paths, this means that the lowest parts of the jets observed by AIA are at heights of 0.06–0.15 $R_{\odot}$.

The times at which the brightening event occurs on the disk in EUVI A images, and the time/height of first appearance in LASCO C2 leads to a simple estimate of a mean speed of the disturbance through the lowest corona, shown as column "EUVI speed" in Table 2. The distance between the lowest corona and the height measured in LASCO C2 is estimated by assuming a radial path placed behind the limb, corresponding to the approximate longitude of the base of the jet in EUVI A.

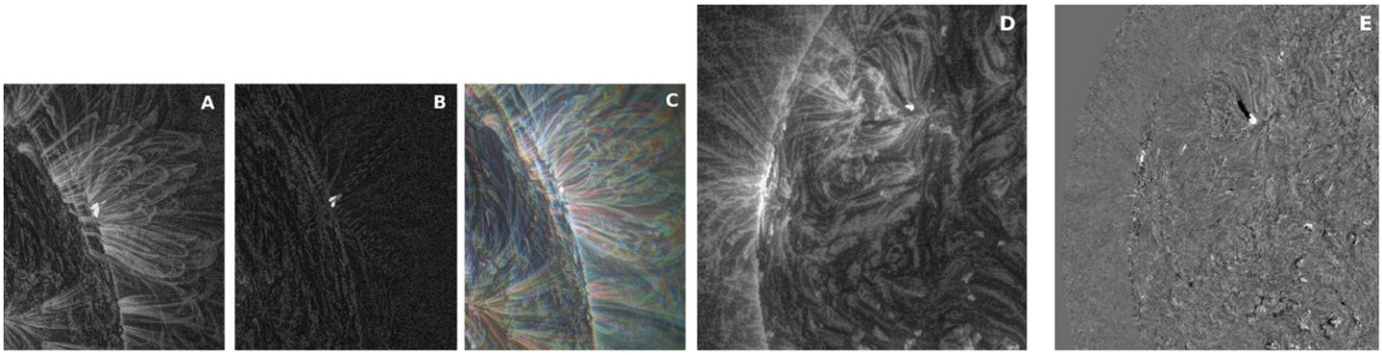

Figure 7. Imp 2 jet event as seen in AIA/*SDO* (A) 171 Å, (B) 304 Å, (C) 171, 193, 211 Å composite and *STEREO A*/EUVI, (D) EUVI A 195 Å, and (E) running difference 195 Å image. AIA 171 Å channel images are dominated by emission from Fe IX ions with a peak formation temperature of ∼0.6 MK, and the 304 Å channel dominated by He II ions at $\sim 5 \times 10^4$ K. The *STEREO* EUVI 194 Å channel observes emission from Fe XII ions at a peak formation temperature of approximately 1.5 MK. The EUV images are processed using Multiscale Gaussian Normalization (MGN; Morgan & Druckmuller 2014). The time-differenced image is made by subtracting a previous image from the image of interest, and dividing by their mean. The event in 304 Å is also available as a movie in the electronic edition of the journal. In addition to the impulsive event shown here, the movie shows shedding of material before the slow event that appears to fall back toward the Sun near this region.

(An animation of this figure is available.)

The "EUVI speeds" have a wide range—ranging from 400 to over 1000 km s^{-1}. The linear speed and acceleration in Table 2 are calculated from LASCO C2 data using a bootstrapping scheme described by Byrne et al. (2013) for a linear fit ("Linear speed") and a 2nd-order fit (giving acceleration).

The timings of the jets, and the height–time profiles of Figure 11 shows that the puffs observed by LASCO C2 are not directly due to either the primary or secondary jets observed in EUV. This is surprising, since the expectation is that the EUV jetting material would lead to the white light puffs. For Imp 6 and 10 in particular, the puffs appear in LASCO C2 at a height of $\sim 2.5\,R_\odot$ as the primary jets reach an apparent (not corrected for projection) height of below $1.5\,R_\odot$. For Imp 3, there is a small time delay between AIA and LASCO C2, but the height–time profile does not suggest alignment between the path of the EUV jet and the white light puffs. The speeds of the primary jets for Imp 2, 3 and 6, estimated using a linear fit to the red points of Figure 11 are on the order of 100 km s^{-1}. Even given the large uncertainties associated with the point-and-click method, this is considerably lower than the linear speed measured in LASCO C2, and is completely inconsistent with the "EUVI speed" parameter listed in Table 2, further confirming the lack of direct connection between the jets and the puffs. COR1A/*STEREO* running-difference images reveal very faintly some of the brighter puffs and confirm that their appearance at low heights ($\sim 1.3\,R_\odot$) is too early to be the jetting material observed in EUV. Therefore the expanding puffs, viewed by the coronagraphs, cannot be a manifestation of the material seen in the EUV jets. The speeds of both the primary and secondary EUV jets tend to decrease with height, and their appearance in the image sequences suggest a parabolic path aligned along the line of sight, similar to the jets described by Zhang & Ji (2014). This strongly suggests that the jets are propagating along large closed-field loops rather than into the extended corona along open field.

Figure 12 shows an estimate of the mass contained in the LASCO C2 dynamic events over the 3 day period. The masses of the event range from $(0.4–3.2) \times 10^{11}$ Kg, and in comparing means are around a factor of 4 times less massive than unstructured CMEs, and a factor of 10 less massive than structured 3-part CMEs arising from filament eruptions as shown by the statistical study of Hutton & Morgan (2015). From the approximate estimate of acceleration and mass, Table 2 lists estimates of force (=*ma*), and of the gravitational force averaged over the range of heights observed by LASCO C2. The final column gives the net force directed outwards. There is no agreement in this estimate of net force between the events, which is perhaps not surprising given the uncertainties involved. Despite this, we can say that all events have quite a high speed in the LASCO C2 FOV, and all are experiencing deceleration.

4. DISCUSSION AND CONCLUSIONS

The puffs observed in white light are most likely a disturbance caused by the initial reconnection event which also drives the first narrow jet. The primary jet, the associated flaring activity, and the puffs are all symptoms of the magnetic reconnection. The jets themselves do not form the puffs, yet they are both caused by the same event. In contrast to the event of Shen et al. (2012), the puffs do not have an obvious flux rope structure—they are just a broad, faint front of enhanced brightness. As such, they are a disturbance caused by the energetic reconnection events, propagating outward from the Sun along open field lines and their "mass," as given in Table 2, gives a measure of the amplitude of the disturbance. The expanding open flux near the AR, as shown in the PFSS model of Figures 5(a) and (b), provides an avenue for the disturbance to propagate into the extended corona.

The slow event is allowed to erupt by the same series of reconnection events which are driving the EUV jets and the white light puffs. The model of Shen et al. (2012) is of relevance to this event, in which narrow reconnection jets are weakening a field which allows a flux rope eruption. The interpretation of the 2013 January 17–19 events should encompass the occurrence of paired jets, the fast puffs and the slow eruption in an unified manner, and the underlying source of the events must be the small region of positive flux embedded in the predominantly negative footpoint of the AR (see Figure 5(c)).

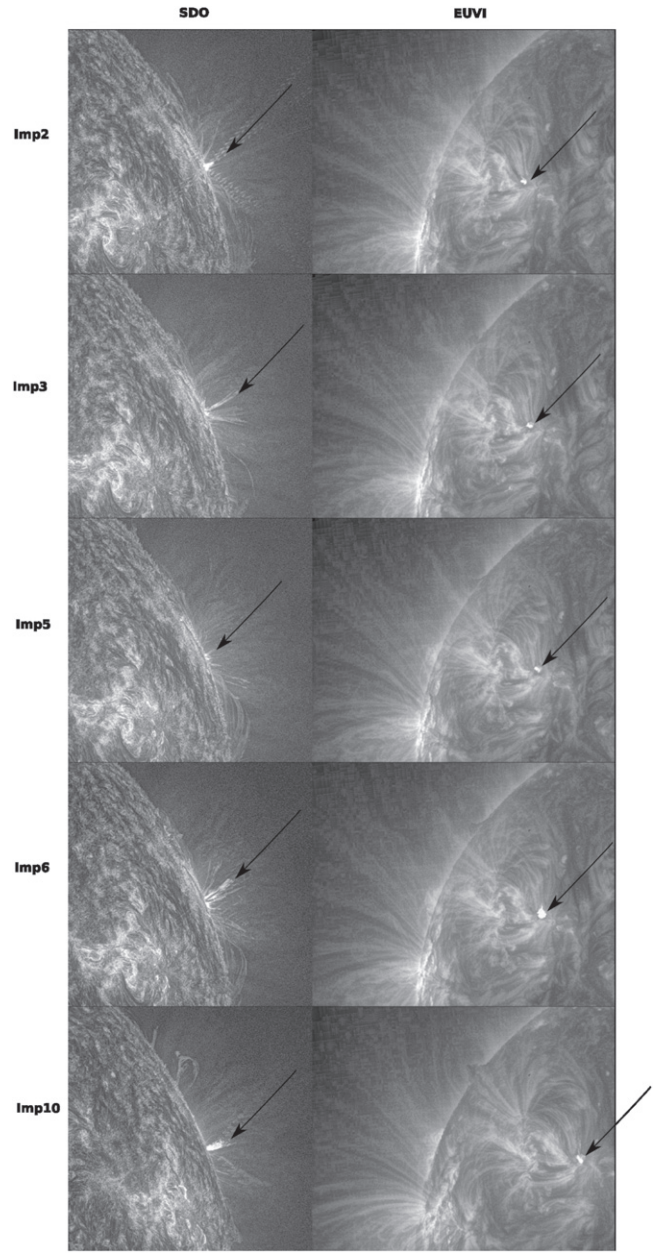

Figure 8. Five of the impulsive events seen in the AIA 304 Å channel (left column) and EUVI A 195 Å channel (right column) for events Imp 2, 3, 5, 6, and 10 (top to bottom). Arrows indicate the region of interest. Flaring and eruption of material is observed in the AIA images while the EUVI images show the brightening on the disk. EUVI running difference images reveal rapid outflow of material, consistent with the AIA images.

The simplest interpretation encompassing all the phenomena is of a typical reconnection between the small region of opposing flux in the AR and the surrounding footpoint field. This causes the observed flares and also drives the primary jets. The reconnection is between closed field loops, so that the large primary jets flow along the main large-scale closed field of the AR, and do not lead to open-field eruptions in the extended corona. Closed–closed reconnection also explains the parabolic trajectory of the EUV jets. The rapid reconfiguration of the field drives a disturbance which propagates outwards, appearing as the puffs in the coronagraph images. As the disturbed AR field lacks equilibrium, a large secondary injection of material (the secondary jet) sometimes occurs. This may be due

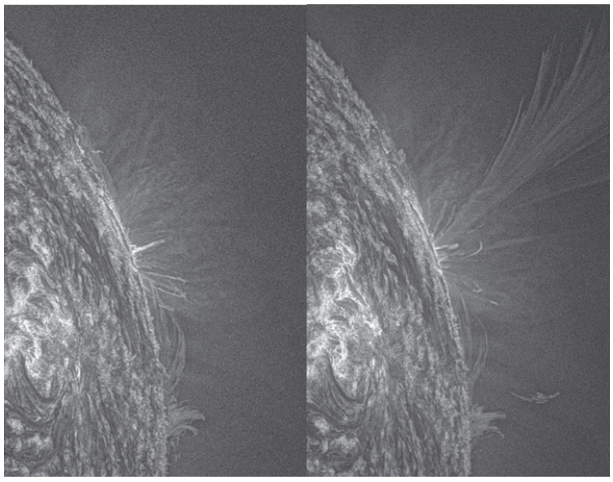

Figure 9. Example of a jet and a post-jet event in the 304 Å channel (Imp 6 event) seen in the AIA 304 Å channel. The primary jet (left) is seen on the limb at 09:42 UT on 2013 January 18. The secondary jet (right) resembles a large spray seen at 10:09 UT.

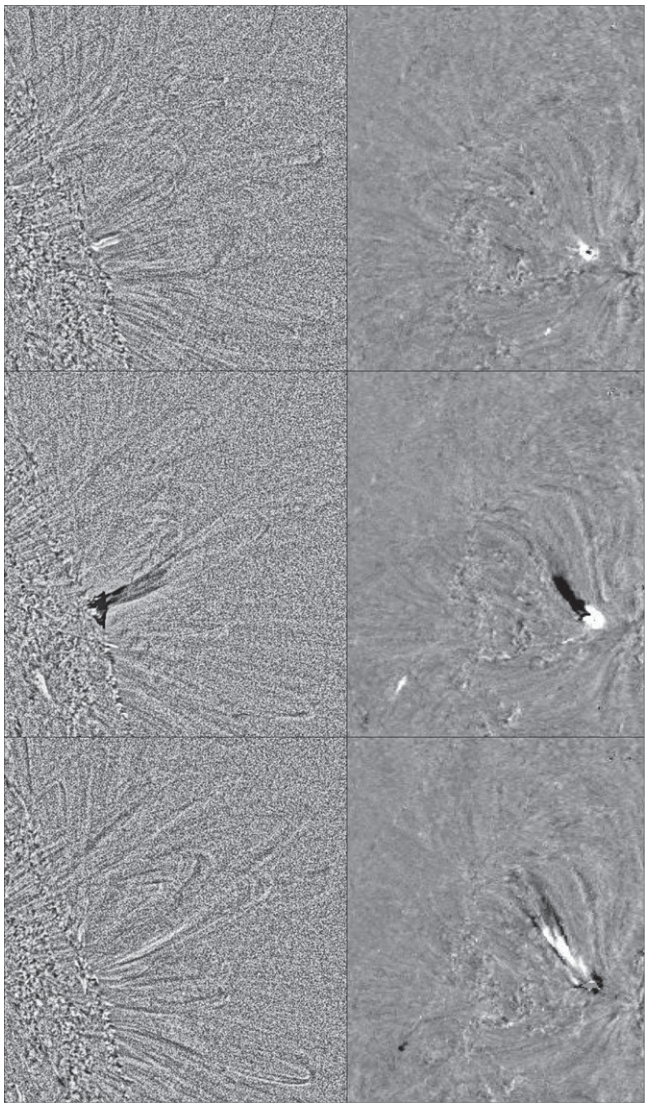

Figure 10. Time-differenced images of the Imp 2 event from AIA 171 Å (left panels) and EUVI 195 Å (right panels) showing three primary phases of this jet pair, as described in the text.

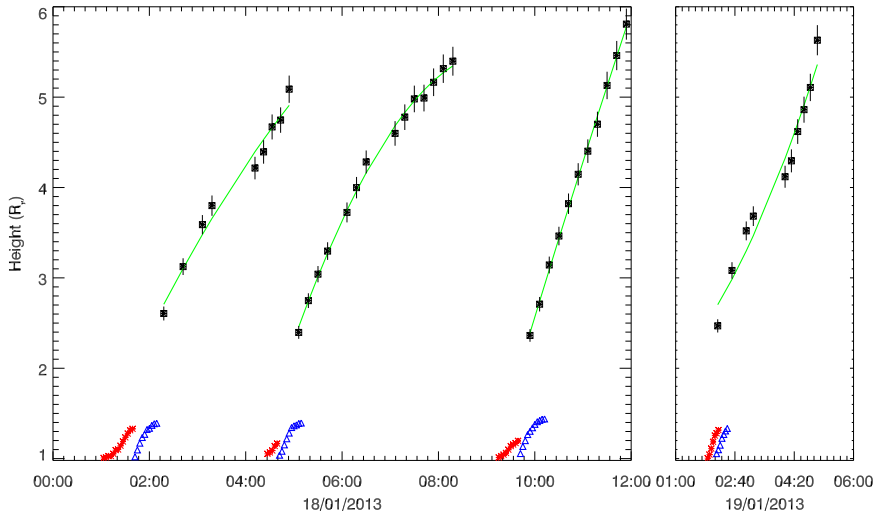

Figure 11. Height–time profiles for four selected events—Imp 2, 3, 6, and 10 in the AIA/*SDO* 304 Å channel (red and blue points), and in LASCO C2 (black points with error bars). This plot concentrates on the four paired-jet events. In each case, the center of the front edge of each eruption is selected through manual point-and-click. The red curves represent an initial narrow jet event, which immediately follows the flare brightening. The blue curves represent a post-jet-like event during which material is pushed outward from the area of the jet a few hundred seconds after the initial event. A second order polynomial fit with errors is shown (green) for the LASCO data. A summary of speeds and other values is shown in Table 2.

to expansion of the initial flux tube by the primary jet or by the general reconfiguration of the field. Evidence for the expansion of the flux tube is supported by the far broader angular extent of the secondary jets compared to the primary jets.

The large-scale closed field which has its footpoints moved within the AR during the reconnection may become unstable due directly to the recurrent reconnection and also due to the recurrent mass flow of the jets, and this may manifest as the slow eruption. The new footpoints of the large-scale closed field may be distant from the original footpoints, extending the field lines and allowing the field to subsequently rise to a more stable state. Once this rising field reaches a critical height, it continues to propagate as a slow CME. Alternatively, the transport of the footpoints of large-scale closed field within the AR may weaken the overlying field, allowing an underlying flux rope to rise, eventually escaping as the slow CME.

Very narrow CMEs are often observed propagating into the extended corona as a consequence of low-coronal jets (e.g., the narrow CME reported by Shen et al. 2012). In the case reported here, the CMEs are not a continuation of the jetting material, but are likely disturbances caused by the initial reconnection event, propagating along an expanding region of open flux adjacent to the large AR. Vourlidas et al. (2013) identified a subset of smaller CMEs as "jet-CMEs," being narrow CMEs of $\leqslant 40^{\circ}$ or less in width lacking a sharp front, detailed sub-structure, or circular morphology. Many such lower-mass (on average), unstructured CMEs are likely caused by the eruption of narrow filaments which do not possess an extended flux-tube structure (or cavity) (Hutton & Morgan 2015) or filament eruptions which occur within pseudostreamers (Wang 2015). Bemporad et al. (2005) report on a new type of narrow CMEs called "streamer puffs." This type of CME is named as such because it travels along a streamer without altering its shape. There is a magnetic arcade under the streamer where flare events lead to the puffs. Similarly, Moore & Sterling (2007) report on the coronal-dimming footprint left behind by a streamer-puff CME. The streamer-puff presented is a result of a magnetic explosion erupting from a "quasi-potential magnetic arch" near a filament or flare. The work by Bemporad et al. (2005) is similar to ours because it presents a series of ejecta that lead to a series of events but the streamer-puffs are more structured plasmoids. In our case, we have a disturbance of the field or a shock without ejection of material (see Figure 3). The event in Moore & Sterling (2007) has the appearance of a flux rope CME whereas our events do not. Our events are far fainter and less structured. The "puff" CMEs reported here are associated with the jets, but are not a direct extension of the jet material. They are instead propagating disturbances caused by the reconnection events in the AR.

This multi-instrument study of a series of fast, faint coronal puffs and a slower, more massive, eruption reveals a small jetting region as the source of both. Summarizing:

1. The series of events are caused by a small region of positive flux embedded within a large negative AR footpoint. Twelve jets/puffs occur over a three-day period, showing a recurrent series of reconnections driven by the island of positive flux. At the height of activity (2013 January 18), jets and puffs occur every three hours or less.
2. The fast puffs are not formed from the ejection material of the jets themselves. This is shown through the timing of their appearance in LASCO C2 and COR1/*STEREO A*, a comparison of their speeds compared to the speeds of the EUV jets, and to a lesser extent by their broad angular range compared to the narrow jets. The fast puffs are likely propagating disturbances (or wave fronts) caused directly by the energetic reconnection events which also cause the EUV jets. The disturbances appear to pass through the overlying coronal structures, including the slow eruption, due to the line of sight effect.
3. The fast coronal puffs have speeds on the order of $300\,\mathrm{km\,s^{-1}}$ in the LASCO C2 FOV, and all show significant deceleration. Their brightness, or mass, are on the order of 10 times smaller than mean 3-part CME mass, and 4 times smaller than mean unstructured CME mass. Their "mass" should be interpreted as the amplitude of a propagating disturbance rather than a flow of material.

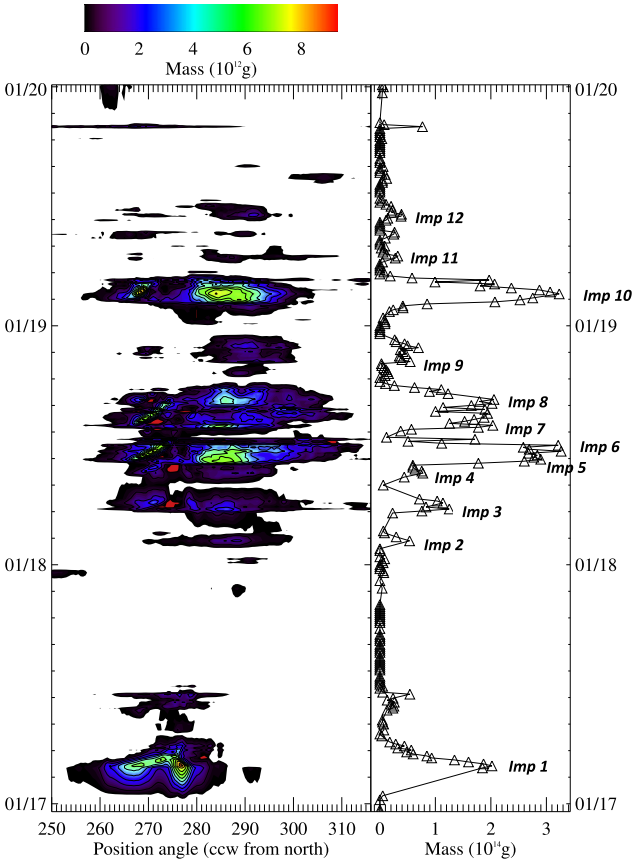

Figure 12. Mass plot for 2013 January 17–19 events, as calculated for LASCO C2 data. The left panel shows mass as a function of position angle and time (integrated over 2.5–5.95 $R_{\odot}$ within the LASCO C2 FOV). The right panel shows mass integrated over the position angle range of interest. Individual peaks correspond to the best estimate of impulsive events, all of which are labeled. For an estimate of masses, the calibration methods and DST are applied to the LASCO C2 data as described by Morgan (2015). An estimate of the mass is then made using a plane-of-sky approximation. There are several large uncertainties in the mass. The plane-of-sky approximation assumes that all emission is from the point of closest approach to the Sun along the line of sight, while the events are all approximately 20°–30° behind the plane-of-sky. This leads to an underestimate of the mass by 5%–10%. A larger uncertainty is the identification and isolation of the CME signal. As shown in Figure 1, some pairs of events may share the LASCO field of view, so their masses may be difficult to separate. Since the events are faint, some of the signal may not be summed due to filtering and thresholding steps in the DST process.

4. Several of the jets occur in clear pairs, with a narrow primary jet and a secondary wider and more massive jet occurring several tens of minutes later. The apparent speeds of these jets are on the order of 100 km s^{-1}, significantly lower than the speed of the puffs observed by LASCO C2. The secondary jets are likely caused by a pressure imbalance following the rapid reconfiguration of field lines and possible expansion of a flux tube caused by the primary jets.
5. The slow event is structured and more massive than the fast puffs, and has a structure suggesting a flux tube. After its very gradual rise into the LASCO C2 FOV, its eventual propagation speed is just over 100 km s^{-1}. Its initial rise seems to be linked to the timing of the fast puffs. This suggests that the recurrent reconnections are allowing the gradual eruption through a weakening of the containing field.

This work shows that propagating disturbances, without an accompanying flow of material, are clearly observable in the extended inner corona. The CME is constrained to erupt by very gradual steps, while the disturbances continue to propagate through the corona and are clearly visible. Such disturbances are likely common, indeed, perhaps they are caused by most flares and jets. They may be difficult to identify since they are usually obscured by an associated CME, or that the disturbance forms the faint front of a 5-part CME (Vourlidas et al. 2013). Great care must therefore be taken in connecting disturbances in the extended corona with events closer to the Sun—not all dynamic events are flux tubes or a true flow of material, particularly for faint, low-"mass" events.

Morgan is grateful for a research fellowship from the Leverhulme Foundation, which made this work possible. He is also grateful to the Coleg Cymraeg Cenedlaethol for funding to Prifysgol Aberystwyth. *GOES* data is provided courtesy of the Space Weather Prediction Center, part of the National Oceanic and Atmospheric Administration (NOAA). The *SDO* data used are provided courtesy of NASA/*SDO* and the AIA science team. The *SOHO*/LASCO data used here are produced by a consortium of the Naval Research Laboratory (USA), Max-Planck-Institut fuer Aeronomie (Germany), Laboratoire d'Astronomie (France), and the University of Birmingham (UK). *SOHO* is a project of international cooperation between ESA and NASA. The *STEREO*/SECCHI project is an international consortium of the Naval Research Laboratory (USA), Lockheed Martin Solar and Astrophysics Lab (USA), NASA Goddard Space Flight Center (USA), Rutherford Appleton Laboratory (UK), University of Birmingham (UK), Max-Planck-Institut fur¨ Sonnen-systemforschung (Germany), Centre Spatial de Liege (Belgium), Institut d'Optique Théorique et Appliqúee (France), and Institut d'Astrophysique Spatiale (France).

APPENDIX

Supplementary movies of the LASCO C2 and *SDO* 304 Å images are available in the electronic edition.

REFERENCES

Alexander, D., & Fletcher, L. 1999, SoPh, 190, 167
Bemporad, A., Sterling, A. C., Moore, R. L., & Poletto, G. 2005, ApJL, 635, L189
Bougeret, J. L., Goetz, K., Kaiser, M. L., et al. 2008, SSRv, 136, 487
Brueckner, G. E., Howard, R. A., Koomen, M. J., et al. 1995, SoPh, 162, 357
Byrne, J. P., Long, D. M., Gallagher, P. T., et al. 2013, A&A, 557, A96
Chen, P. F. 2011, LRSP, 8, 1
Chifor, C., Isobe, H., Mason, H. E., et al. 2008, A&A, 491, 279
Culhane, L., Harra, L. K., Baker, D., et al. 2007, PASJ, 59, S751
Forbes, T. G., & Priest, E. R. 1985, SoPh, 94, 315
Guo, Y., Démoulin, P., Schmieder, B., et al. 2013, A&A, 555, A19
Halain, J.-P., Berghmans, D., Seaton, D. B., et al. 2013, SoPh, 286, 67
Howard, R. A., Moses, J. D., Socker, D. G., Dere, K. P., & Cook, J. W. 2002, AdSpR, 29, 2017
Howard, R. A., Moses, J. D., Vourlidas, A., et al. 2008, SSRv, 136, 67
Hutton, J., & Morgan, H. 2015, ApJ, 813, 35
Kaiser, M. L. 2005, AdSpR, 36, 1483
Lemen, J. R., Title, A. M., Akin, D. J., et al. 2012, SoPh, 275, 17
Li, H. D., Yang, J. Y., Bi, Y., & Liang, H. F. 2015, Ap&SS, 359, 44
Liu, J., Wang, Y., Shen, C., et al. 2015, ApJ, 813, 115
Liu, W., Berger, T. E., Title, A. M., et al. 2011, ApJ, 728, 103
Moore, R. L., Cirtain, J. W., Sterling, A. C., & Falconer, D. A. 2010, ApJ, 720, 757

Moore, R. L., & Sterling, A. C. 2007, ApJ, 661, 543
Moreno-Insertis, F., & Galsgaard, K. 2013, ApJ, 771, 20
Morgan, H. 2015, ApJ, 219, 23
Morgan, H., Byrne, J. P., & Habbal, S. R. 2012, ApJ, 752, 144
Morgan, H., & Druckmuller, M. 2014, SoPh, 289, 2945
Morgan, H., Habbal, S. R., & Woo, R. 2006, SoPh, 236, 263
Nisticò, G., Bothmer, V., Patsourakos, S., & Zimbardo, G. 2009, SoPh, 259, 87
Pariat, E., Antiochos, S. K., & DeVore, C. R. 2009, ApJ, 691, 61
Patsourakos, S., Pariat, E., Vourlidas, A., et al. 2008, ApJL, 680, L73
Pesnell, W. D., Thompson, B. J., & Chamberlain, P. C. 2012, SoPh, 275, 3
Priest, E. 2014, Magnetohydrodynamics of the Sun (Cambridge: Cambridge Univ. Press)
Raouafi, N.-E., Petrie, G. J. D., Norton, A. A., Henney, C. J., & Solanki, S. K. 2008, ApJL, 682, L137
Scherrer, P. H., Schou, J., Bush, R. I., et al. 2012, SoPh, 275, 207
Schou, J., Scherrer, P. H., Bush, R. I., Wachter, R., et al. 2012, SoPh, 229, 207
Seaton, D. B., Berghmans, D., Nicula, B., et al. 2013, SoPh, 286, 43
Sheeley, N. R., Jr., Lee, D. D.-H., Casto, K. P., Wang, Y.-M., & Rich, N. B. 2009, ApJ, 694, 1471
Sheeley, N. R., Jr., & Wang, Y.-M. 2007, ApJ, 655, 1142
Shen, Y., Liu, Y., Su, J., & Deng, Y. 2012, ApJ, 745, 164
Shibata, K., Ishido, Y., Acton, L. W., et al. 1992, PASJ, 44, L173
Shibata, K., Tajma, T., Steinolfson, R. S., & Matsumoto, R. 1989, ApJ, 345, 584
Shimojo, M., Hashimot, S., Shibata, K., et al. 1996, PASJ, 48, 123
Shimojo, M., Narukage, N., Kano, R., et al. 2007, PASJ, 59, S745
Shimojo, M., & Tsuneta, S. 2009, ApJL, 706, L145
Subramanian, S., Madjarska, M. S., & Doyle, J. G. 2010, A&A, 516, A50
Tsuneta, S., Ichimoto, K., Katsukawa, Y., et al. 2008, ApJ, 688, 1374
Vourlidas, A., Buzasi, D., Howard, R. A., & Esfandiari, E. 2002, in Solar Variability: From Core to Outer Frontiers Vol. SP-506, ed. A. Wilson (Noordwijk: ESA), 91
Vourlidas, A., Lynch, B. J., Howard, R. A., & Li, Y. 2013, SoPh, 284, 179
Wang, Y. M. 2015, ApJL, 803, L12
Wang, Y.-M., Sheeley, N. R., Jr., Socker, D. G., et al. 1998, ApJ, 508, 899
Yokoyama, T., & Shibata, K. 1996, PASJ, 48, 353
Yu, H.-S., Jackson, B. V., Buffington, A., et al. 2014, ApJ, 784, 166
Zhang, Q. M., & Ji, H. S. 2014, A&A, 567, A11